Direct contact of bacterial surface induces phase separation of the host phagosome membrane

Aher Jayesh Bhausaheb[1,2], Aniruddha N[2,3], Debraj Koiri[1,2], Jafarulla Shaikh[1,2], Sandeep Choubey[2,3], Mohammed Saleem[1,2,4*]

Affiliations

[1] School of Biological Sciences, National Institute of Science Education & Research (NISER), Bhubaneshwar, India.
[2] Homi Bhabha National Institute (HBNI), Mumbai, India.
[3] Institute of Mathematical Sciences (IMSc), Chennai, India.
[4] Center for Interdisciplinary Sciences, National Institute of Science Education & Research (NISER), Bhubaneshwar, India.

Abstract

Pathogenic bacteria evade host defense by rupturing the phagosomal compartment, enabling their escape into the host cytosol. The bacteria is known to establish direct physical contact with the host compartment prior to phagosome disruption. However, the impact of direct-physical contact on the phagosome remodeling and deformation remains elusive. To probe this, we first developed a method wherein we reconstitute a phagosome-like giant compartment encapsulating *Mycobacterium smegmatis*, a non-motile opportunistic bacterium. We discover that the direct contact between the bacteria and the encapsulating host membrane induces membrane bending, lipid wrapping, and local lipid phase separation at the contact site. The degree of phase separation is driven by the bacterial load leading to fluidization of the membrane, as evident from the decreased area stretch and bending modulus, making the host compartment more deformable. Surprisingly, for saturating bacterial load the fluid host membrane transforms into a scaffold-like rigid layer. We also find that the direct contact of the bacteria enhances the membranolytic potential of ESAT-6 thus contributing to its virulence. Together our findings provide mechanistic insights into the role of direct physical contact of the bacteria during phagosome disruption.

Introduction

The interaction of bacteria with the cellular membrane interfaces is essential for its host entry, intracellular life as well as egress [1]. Such highly complex processes are driven by multiple coordinated protein or lipid-dependent noncovalent interactions[2]. Several invasive bacterial pathogens, such as *Listeria monocytogenes*, *Pseudomonas aeruginosa* are known to hijack host membrane interfaces for actin polymerization resulting in the bacterial engulfment by the host cell membrane[3, 4]. *P. aeruginosa* induces cell membrane invaginations via a lipid zipper formation by the interaction between the glycosphingolipid Gb3 and the bacterial surface lectin LecA, in addition to other cell surface receptors[5]. Clathrin and Arp2/3 complexes have been identified as the key regulator of actin polymerization for zippering pathogens such as *Listeria* and *Yersinia*[6, 7]. Likewise, *Mycobacterium tuberculosis* (*Mtb*)is known to gain entry into the host cell via passive internalization or engulfment mediated by several surface adhesion proteins[8, 9]. The *Mtb* are ejected from the host cell by generating actin-based structures called ejectosomes that are aided by autophagy machinery enabling a non-lytic mechanism [10, 11]. Our understanding of bacterial host entry has been reasonably refined in recent times and mediated by a diverse set of pathogen-specific biochemical interactions. However, the disruption of the pathogen-containing vacuolar compartment of the host cell remains an open question, particularly in the case of *Mtb*[12].

Mtb survives intracellularly by hijacking the phagosome maturation [13, 14]. ESAT-6 (6kDa early secretory antigen target), a highly immunogenic effector protein secreted by *Mtb*, is critical for the process of phagosome (also referred to as Mycobacteria containing vacuole (MCV)) rupture [15, 16]. Purified recombinant ESAT-6 is known to induce lysis of cultured macrophages through permeabilization of both the phagosome membrane as well as cell membrane upon gaining access to the cytoplasm [17-19]. Despite significant evidence that supports the direct role of ESAT-6 in phagosome lysis and virulence[20-22], a recent study reported that ESAT-6 interaction alone is not sufficient for phagosome disruption. Instead direct bacterial physical contact is important for gross phagosomal membrane disruption [23]. *In vivo* observations also suggest that ESAT-6 required additional factors such as the lipid phthiocerol dimycocerosates (PDIMs), which are complex branched cell-wall-associated lipids known to induce sterol clustering in host membranes, eventually inducing phagosome disruption [24-28]. Interestingly, *Mycobacterium marinum* transposon mutants induce phagosome damage despite their inability to secrete ESAT-6, suggesting that ESAT-6 alone may not be sufficient for the ESX-1 virulence function [29]. Though the ability to damage the phagosomal membrane has emerged central to *Mtb* virulence, the mechanism of phagosome membrane remodeling and disruption remains poorly understood [12]. *Mtb* is known to be a non-motile bacteria, however, exhibits sliding mobility upon encountering surfaces. Very recently, motile swimming bacteria such as *E. coli* and *B. subtilis* have been shown to induce non-equilibrium membrane fluctuations [30], deformations [31] as well as conferring coupled mobility in synthetic giant vesicles encapsulating the bacteria[32]. However, the dynamics and impact of direct physical contact of a non-motile bacteria with the vacuolar compartment remain unknown to date. Understanding the implications of direct physical contact of the bacteria is not only important for vacuolar

disruption but also for a broad class of bacterial pathogens interaction with host cell membranes both during internalization as well as egress.

In this work, we developed an *in vitro* reconstitution method to dissect the mechanism of phagosome membrane remodeling induced by the direct physical contact of bacteria by encapsulating live *Mycobacterium smegmatis* (as a model non-motile opportunistic bacteria) inside a host phagosome-like compartment. *Mycobacterium smegmatis* allows us to dissect both the behavior of a non-motile bacteria exhibiting sliding mobility under a confined environment. Further, it also enables us to delineate the role of direct physical contact in phagosome membrane remodeling from virulence factors. We capture the dynamics of bacterial direct contact as well as bacterial-load-mediated host membrane remodeling. We discover that the direct-contact of the *M. smegmatis* with the encapsulating host membrane results in significant lipid wrapping, membrane bending, and local lipid phase separation at the contact site. In contrast, the higher bacterial load induces complete lipid phase separation of the compartment. The lipid wrapping is driven by the surface condensation of the compartmental lipids onto the bacterial surface in direct contact and hinders host lipid diffusion by two-fold at the contact area. The direct physical contact decreases the area stretch and bending modulus of the host membrane, thus, making the host compartment more deformable. The degree of bending and area expansion of the phagosome-like compartment is dictated by the ratio of the compartmental surface area available to the surface area of the bacterial contact site. Further direct contact of the bacteria enhances the membranolytic potential of ESAT-6 thus contributing to its virulence.

RESULTS

Direct contact of the *Mycobacterium smegmatis* induces lipid wrapping and creates diffusion barriers in the host membrane

To examine the role of direct contact of bacteria on the host phagosomal membrane shaping and remodeling, we developed a method to encapsulate live bacteria inside giant unilamellar vesicles composed of phagosomal membrane lipids (as described in methods and Fig 1a, b). We optimized electroformation to encapsulate live fluorescent bacteria. This method reduces the impact of external impurities such as oil and ensures reliable interaction with host membranes. We used GFP - *M. smegmatis* as a model organism to understand the role of bacterial direct-contact mediated membrane remodeling in the absence of any secretory virulence factors like ESAT-6. Despite being avirulent, the fast-growing *M. smegmatis* is considered an ideal surrogate for mycobacterial research[33]. We first quantified the viability of the bacteria in the experimental conditions through colony forming unit (CFU) assay and found it to be around 60% (Fig.1c). To capture the dynamics of bacterial interaction in real-time, live bacteria were encapsulated in phagosome membrane mimic GUVs labeled with 0.1% Rhodamine-PE (Rh-PE) and were immobilized using 0.03% Biotinylated-PEG. Upon monitoring over 60 min, suspended bacteria were found to exhibit random Brownian motion inside the reconstituted phagosome. Interestingly, the area of contact between the bacteria and the host membrane showed an accumulation of host lipids (Fig.1e, S1). Upon visualizing the GUV in 3D at different planes (Fig.1f), we observed lipid wrapping over the bacterial surface area as also illustrated in the schematic diagram (Fig.1d). Such interaction induces membrane bending at the contact area. Furthermore, the fluorescence recovery of Rh-PE at the contact area is reduced by two-fold after photobleaching (Fig.1g), hinting that the strong inter-surface interaction between host and bacteria creates a diffusion barrier. This subsequently leads to lipid segregation within the host membrane. To track the change in lipid reorganization and packaging, we employed two dye model systems (Rh-PE in red and Top-fluor cholesterol in green) and monitored their fluorescence intensity over time (Fig.1h, S2, S3). We observed that the fluorescence intensity of Top-fluor cholesterol decreases in the vicinity of the contact area (Fig. 1i, k). In contrast, the fluorescence intensity of Rh-PE increases near the contact area, as shown in zoomed images (Fig.1 j, l). Together the bacterial direct-contact induces membrane bending, lipid wrapping at the contact area and creates a diffusion barrier resulting in the reorganization of the lipids and change in lipid packing as evident from the marked increase in the fluorescence intensity of Rh-PE suggesting disorderliness in the region [34].

Moderate mycobacterial load induces fluidization and phase separation in the host membrane.

We next investigated whether the replicating bacterium inside the phagosome affects phagosome membrane dynamics. To capture this, we encapsulated an increased load of bacteria inside the GUV, as illustrated in the schematic (Fig. 2a). We observed that without bacterial load, Rh-PE fluorescence intensity appears to be homogenous throughout the equatorial plane of the membrane. In sharp contrast, in a moderately loaded condition, the bacteria induce striking phase separation in phagosome like compartments as evident from the Rh-PE signal that is restricted to bacterial

contact areas (Fig.2b). Notably, we observed a change in the fluorescence intensity and thickness of the membrane upon monitoring the GUV containing a moderate bacterial load for 60 minutes (Fig. 2c, S4). Specifically, there is significant mobilization of Rh-PE towards the bottom of the GUV after 60 minutes where the larger pool of bacteria settles down (Fig. 2d, bottom right panel XZ plane). Also, the accumulation of lipids at the bottom of GUVs induces budding at the bottom (Fig. 2d-f). This suggests that bacteria make the membrane more disordered at the contact areas. Likewise, the diffusion of Rh-PE on the membrane partially slowed down as evident from the fluorescence recovery after photobleaching at the equatorial plane (Fig. 2f). Super-resolution microscopy revealed that the weak interactions caused by the bacteria hitting and retracting off the host membrane induced higher disorderliness at the point of contact in the GUVs (Fig. 2 g) as seen from the Rh-PE signal at the equatorial plane (Fig. 2h). Interestingly, the membrane sustained the disorderliness despite the bacteria having retracted after hitting the surface and were no more in contact. These observations collectively suggest that increasing bacterial load inside the GUV results in stronger interactions with the host membrane via Brownian motion affecting the lipid packing. This subsequently leads to phase separation and the mobilization of Rh-PE at the bottom as more stable contacts get established as the bacteria settles to the bottom. This might also impact the mobility of the lipids at other planes as a result of stretching and lipid reorganization in the membrane.

High mycobacterial load drives host membrane remodelling via bacterial surface-induced condensation

The behavior of the Mycobacteria inside the confined volume of mycobacterial-containing vacuole as it replicates particularly with regard to establishing membrane contacts remains unknown [16]. We hypothesized that a substantial increase in mycobacterial load resembling the formation of bacterial clumps within the phagosome [35] would induce a higher probability of establishing direct-contact with the phagosomal membrane. To examine the impact of clump formation on the phagosome membrane, we encapsulated a significantly higher load of mycobacteria, thereby increasing the contact area with the membrane, as illustrated in the schematic (Fig. 3a). To capture the interactions in real-time, we monitored the higher load of GFP- *M. smegmatis* encapsulated inside GUV for 60 minutes. Striking membrane tampering is induced by the random attachment of the bacteria (Fig. 3b, S5). Interestingly, the host membrane remains permanently bent even in the case where the bacteria tend to retract away from their initial contact area. The bacteria exhibit collective mobility as clumps under a higher load compared to that of the moderate load condition. In line with previous observations, we noted the accumulation of lipids at the bottom of the membrane after 60 minutes (Supplementary Fig 1a, b), and subsequent budding at the bottom of the GUV. The budding phenomenon results from phase separation, where the reorganization and mobilization of liquid-disordered lipids induce localized membrane curvature at contact areas making the membrane more deformable (Supplementary Fig 1a, b). To establish the phase separation, we used two dye systems as previously described, and observed an intense phase separation of the host membrane by the bacteria (Fig 3c). Next, to visualize the changes in smaller-sized GUVs similar to

225 phagosome size, we encapsulated 4-6 bacteria within smaller GUVs around size 8-10µm.
226 Remarkably, we found that the bacteria caused complete deformation of the membrane, as
227 illustrated in (supplementary 1c, d). This observation indicates that in smaller GUVs, a higher
228 bacterial load contact area leads to a significantly greater degree of host membrane deformation
229 compared to larger GUVs. This suggests a size-dependent effect, where the smaller volume and
230 surface area of the GUVs amplify the impact of bacterial interactions, resulting in more pronounced
231 membrane deformations. Super-resolution microscopy reveals the host membrane becomes more
232 disordered at the contact area of the bacteria. The white spots indicate the colocalization point,
233 where the bacteria and host membrane are in contact (Fig. 3 d) as evident from the intensity of the
234 overlapping regions of the host and the bacteria (Fig. 3 e). Further, the shape of the bacterial clump
235 appears to drive the shape of the host membrane via stretching (Fig. 3 f). To investigate the role of
236 bacterial surface on the phase separation of the host lipid membrane, we used a two-dimensional
237 Ising model, where the two states (-1 and +1) represent the lipid ordered and disordered states.
238 Bacterial contacts on the membrane were considered as patches where one kind of lipid has a high
239 probability of accumulating (see Supplementary information for details). We find that when the
240 contacts are few (low bacterial load), global phase separation does not occur. However, the
241 membrane can exhibit local phase separation in the vicinity of the contact site (Fig. 3g). Interestingly,
242 increasing the number of contacts (high bacterial load) can drive the entire membrane to phase
243 separate (Fig. 3h). The phase separation intensifies as the bacterial contact area on the membrane
244 increases, becoming significantly more pronounced (Fig. 3i). However, increasing the size of
245 bacterial contact on the membrane, keeping the fraction of total area in contact constant, results in
246 a decrease in the degree of phase separation (Fig. 3j-l). This is a consequence of the bacteria-
247 inducing local phase separation. As more bacteria come closer together, there is a significant overlap
248 in the locally phase-separated regions, thereby diminishing the effect on the entire membrane.
249 Bacterial contact-induced phase separation is more pronounced when the lipid interactions are such
250 that the membrane is near the demixing critical point. (Supplementary 3 b, supplementary text).
251 This suggests that the probability of interaction between bacterial surfaces and the host membrane
252 is influenced by the size of the phagosomal compartment. The disorderliness and degree of phase
253 separation within the membrane are driven by the percentage of bacteria in contact, leading to
254 increased membrane fluidity. As the number of bacteria within a confined volume increases, the
255 probability of interaction and the formation of bacterial clumps also rise. The morphology of the
256 vesicle is determined by the shape of these bacterial clumps (Fig. 3b, f & Supplementary Fig. 1c-d).
257 Further, the fluidized membrane conforms to and wraps around the clumps, resulting in a more rigid
258 scaffold-like structure. Collectively, these concurrent processes are likely to significantly impact
259 membrane parameters.
260
261
262 ## Direct contact of mycobacteria enhances the virulence of ESAT-6
263 We next questioned if there is any correlation between the bacterial load inside the host membrane
264 and the change in the membrane parameters (Fig 4). To test this we used micropipette aspiration
265 to aspirate GUVs encapsulating varying loads of the bacteria. The presence of Mycobacteria inside

266 the GUVs was confirmed through bright-field microscopy. Depending on the mobility of the bacteria
267 and shape fluctuation of the GUV, we broadly classified GUVs into moderate and high load
268 conditions (Fig S6, S7, S8). Moderately loaded bacteria seem to exhibit higher membrane
269 fluctuations and bacterial motion compared to the highly loaded and unloaded conditions (i.e.,
270 without bacteria) (Fig S6, S7, S8). Simultaneously, the geometry (aspiration length L_p and vesical
271 radius R_v, see Fig 4 a, b, c) of the GUV was monitored to document changes in membrane parameters
272 by the interaction of bacteria with the host membrane. Increasing the bacterial load inside the GUV
273 results in a higher probability of establishing bacterial contact with the host membrane as seen in
274 Fig. 2, 3. To quantify these changes in membrane properties, we aspirated moderately loaded GUV
275 with a constant change in pressure (i.e., ΔP= 50 Pa). We observed the aspiration length Lp increases
276 significantly in moderate load as compared to unloaded condition (without bacteria) (Fig 4 a, b, d).
277 Moderate bacterial load is found to reduce the area stretch modulus by 5 folds as compared to the
278 unloaded condition (Fig 4 e). Likewise, the bending modulus of the host membrane is reduced by 6
279 folds as compared to the unloaded condition (Fig 4 f). Surprisingly, no change in L_p is observed for
280 the high load condition (Fig 4 c, d). The aspiration length (L_p = 0) suggests an absence of direct area
281 expansion, precluding the calculation of both area stretch modulus and bending modulus.
282 Interestingly, significant deposition of host membrane lipid is observed over the surface of the
283 pipette (Fig 4 C, S8). This observation suggests that as the bacterial load increases, the fluidity of the
284 host membrane also increases, leading to greater membrane deformability. In contrast, under high
285 load conditions, bacteria aggregate to form a solid-like surface. The fluidized host membrane,
286 influenced by bacterial activity, then wraps around this clump. This interaction collectively results
287 in increased membrane rigidity. These bacterial interactions are efficient in remodeling the
288 membrane properties but are not sufficient for the bacteria to escape from the phagosome
289 membrane.
290
291 Furthermore, to investigate the role of virulent secretory proteins in bacterial escape, we treated
292 these three conditions with a low concentration of monomeric ESAT-6 protein and monitored them
293 for 2 hours. Interestingly, we observed that in this low concentration and the absence of bacteria,
294 there was no significant change in the membrane shape (Fig. 4g, S9). However, under moderate
295 bacterial load, significant budding in the membrane was observed after 60 minutes (Fig. 4h, S10).
296 As observed in the previous experiment, under a high bacterial load, the GUV membrane became
297 more rigid compared to the moderate load (Fig. 4c), creating favorable conditions for membrane
298 rupture and bacterial escape from the phagosome. Subsequent treatment with ESAT-6 induces
299 phagosome membrane rupture resulting in bacterial escape (Fig. 4i, Supplementary Fig. 3a, b, S11).
300 This indicates that bacterial load enhances the membranolytic activity of the virulence factors. The
301 proposed model suggests that direct contact with Mycobacteria affects the maturation of the
302 Mycobacteria-containing vacuole (MCV). This interaction reduces the bending rigidity of the MCV
303 membrane, potentially enhancing ESAT-6-mediated membrane disruption in a bacterial load-
304 dependent manner.

305 ## Discussion

306 Subversion of host membrane functions by secretory effector proteins is identified in several
307 intracellular pathogens. However, the role of direct physical contact of the bacteria with the host
308 membrane and the underlying governing principles of the subsequent membrane manipulation
309 remains unknown [1]. In this study, we reconstitute a non-motile live opportunistic *Mycobacterium*
310 *smegmatis* encapsulated by a phagosome-like giant vesicular compartment. We capture the
311 dynamics of interaction with the membrane in real-time. Intracellular vacuolar compartments
312 represent soft confinements that can be subjected to remodeling and deformation by localized
313 forces such as the active propulsion by motile bacteria. However, whether the direct-contact of the
314 non-motile bacteria can do the same to escape out of the vacuolar compartment remains unknown.
315 We demonstrate that indeed encapsulated non-motile live mycobacteria upon local direct-contact
316 induces membrane bending and lipid wrapping at the area of contact (Fig 1e, f). Further, the contact
317 regions showed a reduction in the diffusion of the host membrane lipids suggesting the creation of
318 diffusion barriers (Fig 1g). Such diffusion barrier-mediated phase separation [36] likely triggered the
319 lipid reorganization at the area of contact, making the membrane more disordered (Fig 1 h-l). The
320 change in the Rh-PE and Top-Fluor Cholesterol signal suggests that the bacteria may be extracting
321 cholesterol from the host membrane as *Mycobacteria* are also known to scavenge cholesterol from
322 the host for their metabolism [37]. Interestingly, the degree of phase separation induced in the host
323 membrane also depends on the mycobacterial load (Fig. 1h-i, 2b-d, 3c-e). Moderate load of freely
324 moving bacteria making direct-contact in multiple plains induced membrane disorderliness and
325 fluidization resulting in protruding buds invaginating from the base of the GUV (Fig 2d-f). Unlike the
326 non-motile mycobacteria, self-propelling motile bacteria are known to induce stronger non-
327 equilibrium fluctuations in the membrane, resulting in the formation of long protruding tubes [30]. In
328 contrast, the higher bacterial load results in gross reshaping of host membrane driven by the direct-
329 contact and clump formation of the bacteria. We think despite lacking self-propulsive forces, direct-
330 contact mediated deformation in the host membrane is driven by inter-surface interactions and
331 dictated by the ratio of available surface area of the host membrane and the area of direct-contact
332 (Fig. 3b, Supplementary Fig 1c-d). Load dependent shape deformations of encapsulated giant
333 vesicles have also been observed for self-propelled janus colloids that induce highly branched
334 tether-like protrusions at low/moderate loads and globular reshaping at higher loads capturing
335 vesicle shapes that do not exist in equilibrium systems [38]. The stoichiometry of the phagosome
336 membrane composition might be mimicked by a ternary lipid composition that is close to demixing
337 point, however, does not phase separate by itself (Fig. 2b). For a given bacterial load, the phase
338 separation of lipids is pronounced when the membrane is near its demixing critical point
339 (Supplementary fig 3a, b). Indeed, previous studies [39-43] have suggested that cell membranes lie
340 close to the demixing critical point[44]. Bacterial surface may induce condensation of host membrane
341 interfaces that are close to the demixing point driving phase separation. Such a phenomena might
342 also explain the lipid zippering proposed for bacterial surface lectin LecA with the host cell
343 glycosphingolipid Gb3 sufficient for driving complete internalization of the *Pseudomonas*
344 *aeruginosa* [5].
345

346 The striking change in the area stretch modulus and the bending modulus of the compartmental
347 membrane with respect to the bacterial load not only renders it more deformable but also might
348 influence the dynamics of phagosome maturation (Fig. 4a-f). Consequently, the activity of ESAT-6 is
349 also induced by these changes in membrane properties. As the bacterial load increases, the
350 membrane becomes more disordered. At moderate bacterial load, ESAT-6 activity induces
351 membrane budding, reducing the available area of the host membrane (Fig. 4h). thus, eventually
352 progressing into a high bacterial load condition (Fig. 4i). This ultimately leads to phagosome rupture,
353 similar to the effects observed under high bacterial load conditions (Fig. 4i). The ESX-1 secretion
354 system facilitates mycobacterial membrane damage by directly interacting with host membranes[23],
355 and targeting sterol-rich microdomains to disrupt the Mycobacterium-Containing Vacuole (MCV)[45].
356 Emerging evidence suggests that the collective properties of the cellular membranes play a crucial
357 role in dictating the binding, assembly as well as functions of numerous proteins [46]. The bending
358 modulus and tension of the membrane regulate the shape generation of the membrane during
359 endocytosis as well as the rate of budding for inter-organelle trafficking[47-49]. The direct-contact
360 mediated manipulation of the vacuolar compartment might have implications for the dynamics of
361 phagosome maturation machinery. For instance, a reduction in the bending rigidity of the
362 phagosome membrane can facilitate and precede the ESAT-6-mediated vacuolar membrane
363 disruption. Further, the changes in the properties of the phagosomal membrane might also
364 influence the dynamics of Rab 5 binding, essential for the initiation of the maturation process.
365 Indeed, the binding of Ras family proteins is known to be sensitive to membrane tension [47, 50]. The
366 mechanical properties of the membranes are critical for processes involving fission and fusion of
367 membranes [48, 51, 52]. Together, we quantitatively show that changes in host membrane parameters
368 as a result of direct contact with bacteria may play a crucial role in delaying phagosome maturation
369 or disrupting phagosome.
370
371
372
373
374
375
376
377
378
379
380
381
382
383
384
385
386
387

Material & Methods

Materials

1,2-Dioleoyl-sn-glycero-3-phosphocholine (DOPC), 1,2-dioleoyl-sn-glycero-3-phosphoethanolamine (DOPE), BSM, di-stearoyl phosphatidyl ethanolamine-PEG (2000)-biotin, and cholesterol were obtained from Avanti Polar Lipids. The fluorescent lipid lissamine rhodamine B sulfonyl (Liss Rhod PE) and Top-fluor cholesterol were also sourced from Avanti Polar Lipids. Avidin-coated chamber slides were acquired from Sigma-Aldrich.

Preparation of GUV

Giant unilamellar vesicles (GUVs) that imitate the phagosomal membrane were made up of 40% DOPC, 5.5% DOPE, 22% BSM, 32.5% cholesterol, 0.03% PEG-Biotin, and 0.1% Rhod PE. GUVs were created by getting and slightly altering the protocol given in[48]. In summary, conductive ITO-coated glass from Nanion Technologies, GmbH was equally covered with 15µL of the lipid mixture at a concentration of 5 mg/ml, and it was vacuum-dried for a minimum of three hours. After rehydrating the dried lipid film in 300 ± 5 mOsm sucrose solution of pH (6-6.5), the GUVs developed for three hours at 40-45°C with a sine voltage of 2V and 10 Hz. Using 7H9 media containing precultured Mycobacteria, the lipid film was rehydrated in order to encapsulate live Mycobacteria within the GUVs.

Microscopy

An 8-well Ibidi chamber slide was coated with 10µl of 1 mg/ml streptavidin, followed by the addition of 200µL of biotinylated GUVs. The GUVs were then incubated for 15 minutes to cause immobilisation. Leica TCS SP8 LCSM imaging was carried out with the proper Rhodamine-PE (561 nm) and Alexa-488 (488 nm) laser. Every experiment was conducted using the same laser power and gain settings.

Initially, images were taken with a lower laser intensity for the Fluorescence Recovery after Photobleaching (FRAP) measurements. A 5µm radius of bleaching was achieved within the chosen ROI after 30 seconds of photobleaching at maximum laser power. The recovery curve was then measured, and the laser intensity was adjusted to the attenuated level. The GUV under visualisation was photobleached at its equatorial plane. Following three repetitions, the FRAP curves were standardised for each condition.

Expression and Purification of ESAT-6

The ESAT-6 protein was expressed using the Escherichia coli BL21 (DE3, pLysS) strain. The strain was transformed with the plasmid pET22b containing the *Mycobacterium tuberculosis* gene Rv3875, which encodes the ESAT-6 protein. Transformed cells were grown in Luria-Bertani (LB) medium at 37°C until the optical density at 600 nm (OD600) reached approximately 0.6. Protein expression was induced by adding 1 mM isopropyl β-D-1-thiogalactopyranoside (IPTG), followed by overnight incubation at 18°C. Post-induction, the bacterial cells were harvested by centrifugation and lysed via sonication. The cell lysate was then subjected to affinity purification using nickel-nitrilotriacetic acid (Ni-NTA) resin, per the manufacturer's instructions (GE Healthcare, UK). The eluted fractions containing the His-6-tagged ESAT-6 protein were analyzed using SDS-PAGE to confirm protein purity. Purified fractions were subsequently dialyzed against an appropriate buffer, concentrated, and stored at -80°C in aliquots for further use.

434 **Micropipette Aspiration**

435 Using a 100X objective lens, all measurements were made using an Olympus IX83 epifluorescence
436 microscope fitted with Hoffman modulation optics. Three-axis hydraulic micromanipulators are
437 utilised to position the pipette. Capillaries with a diameter of 10µm are used to extract micro-
438 pipettes (Narashige Micro Forge MF-900, Sutter Instruments CO P-87). On top of the unfinished DIY
439 coverslip, 100 µl of GUVs were put. The suction pressure P applied to a bilayer vesicle produces a
440 uniform membrane tension (τ), which is described by a geometric relation based on the pipet
441 (Radius)$R_{pipette}$ and vesicle (Radius)R_{GUV} of the vesicle spherical segment exterior to the pipette,
442
443 $$\tau = (1/2)*(R_{pipette}\Delta P)/(1-(R_{pipette}/R_{GUV}))$$
444
445 [53, 54]. Movement of the projection length L_p inside the pipette directly measures the area increase.
446 Using measurements of the vesicle spherical segment and cylindrical projection dimensions, we
447 numerically computed changes in apparent area Δa for each displacement ΔL_p of the projection
448 length with simple geometric formulae and the constraint of a fixed vesicle volume [55]. The
449 proportionality between apparent area and length is easily seen in the following first-order
450 approximation:
451
452 $$\Delta a = 2\pi * R_{pipette} * \Delta L_p + 2\pi R_{pipette}^2$$
453
454 While the reference area $a_0 = 4\pi * R_{GUV}^2$ corresponds to a spherical vesical radius $R_{GUV.}$ These formulas
455 combine to give the following expression for the areal strain:
456
457 $$\Delta a/a_0 = (R_{pipette}^2 * (1+L_p/ R_{pipette}))/2R_{GUV}^2$$
458
459 Displacement of the projection length of an aspirated vesicle under a change in suction pressure is
460 shown in Fig.4d. Even though the apparent area can be measured over a tension range from 76
461 µN/m to 550 µN/m as demonstrated in Fig. 4e to determine the area stretch modulus (K_a), we plot
462 the change in tension (τ) against direct area of expansion, and the resulting slope is $K_{a.}$to determine
463 the bending modulus (K_b), we plot the semi-log of tension(τ) against the direct area of expansion,
464 and resulting slope is $K_{b.}$ All the experiments were performed at room temperature[55].
465

466 **Image Analysis**

467 Image analysis and processing were done using the ImageJ program. The average fluorescence
468 intensity was quantified using the line intensity profiling at the direct contact sites along the
469 equatorial plane of GUVs. The same detection configuration was followed for every experiment.
470 Every experiment set used the same detection configuration. ImageJ was used to manually quantify
471 the diameters of the vesicles.
472
473
474
475
476
477
478
479
480

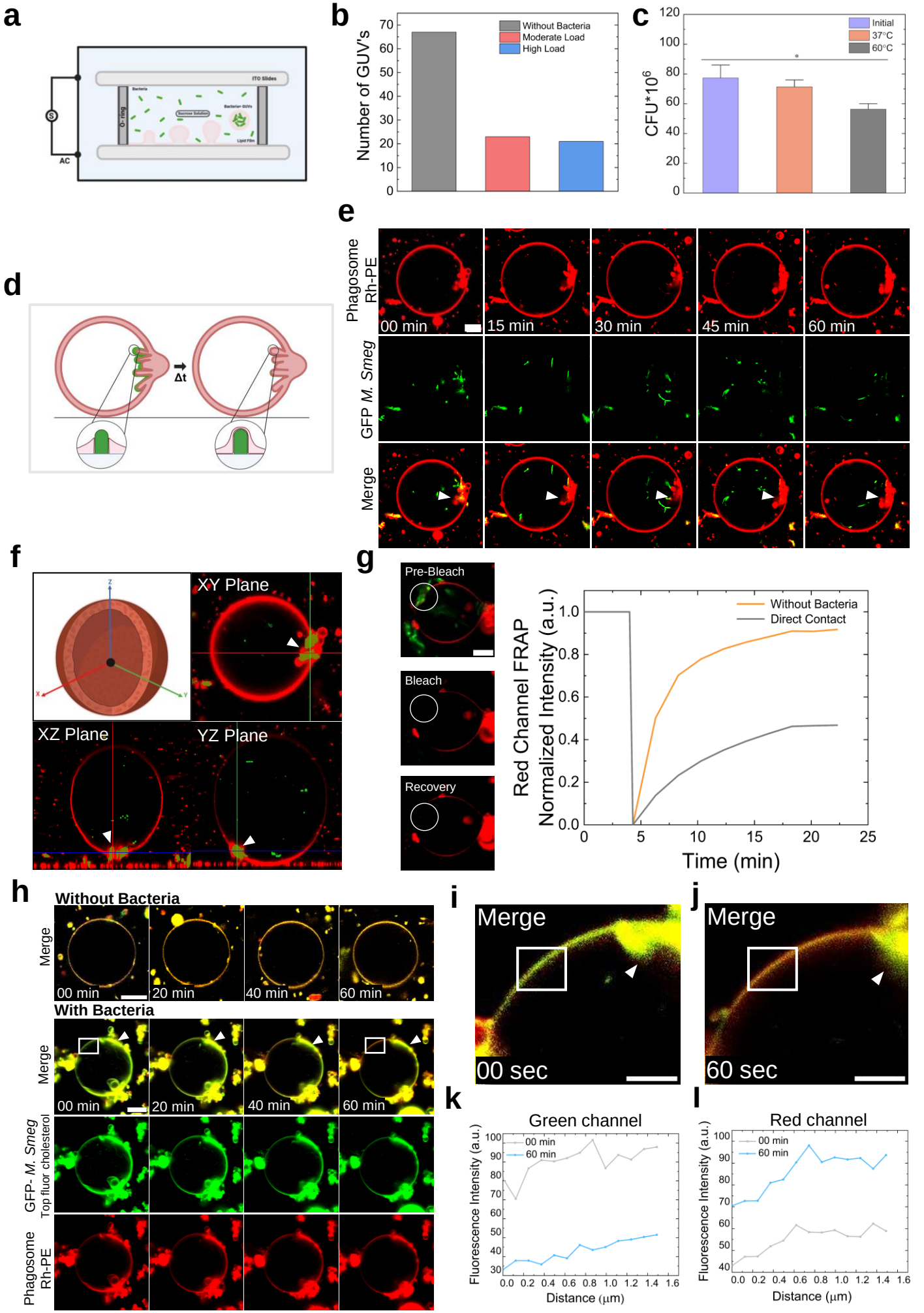
a
ITO Slides
Bacteria
O- ring
Sucrose Solution
Bacteria- GUVs
Lipid Film
S
AC
b
Number of GUV's
Without Bacteria
Moderate Load
High Load
c
CFU*10^6
Initial
37°C
60°C
d
Δt
e
Phagosome Rh-PE
GFP M. Smeg
Merge
00 min
15 min
30 min
45 min
60 min
f
XY Plane
XZ Plane
YZ Plane
g
Pre-Bleach
Bleach
Recovery
Red Channel FRAP Normalized Intensity (a.u.)
Without Bacteria
Direct Contact
Time (min)
h
Without Bacteria
With Bacteria
Merge
GFP- M. Smeg Top fluor cholesterol
Phagosome Rh-PE
00 min
20 min
40 min
60 min
i
Merge
00 sec
j
Merge
60 sec
k
Green channel
Fluorescence Intensity (a.u.)
Distance (μm)
l
Red channel
Fluorescence Intensity (a.u.)
Distance (μm)

481 **Figure Legends**
482
483
484 **Fig 1**
485 Direct interaction with *Mycobacterium smegmatis* triggers lipid wrapping and establishes diffusion
486 barriers in the host membrane
487
488 **a.** Schematic representation of experimental design depicting electroformation and encapsulation
489 of bacteria inside the GUV mimicking the phagosomal membrane. **b.** Statistical analysis of the
490 encapsulated bacteria at variable load conditions (no. of GUVs = more than 100). **c.** Viability of the
491 encapsulated *Mycobacterium smegmatis* quantified by colony-forming units at different
492 temperatures to mimic conditions similar to electroformation. Data shown as Mean ± SD. (*p<0.005
493 in one-way ANOVA) **d.** Schematic representation for the experimental design depicting the impact
494 of direct contact on immobilized GUV mimicking host phagosomal membrane. **e.** Time-lapse
495 confocal imaging of GUVs labelled with 0.1% Rh-PE (red) and immobilized using 0.03% PEG-Biotin
496 encapsulated with live *M. smegmatis* (green). Scale bar, 10µm. Representative images from
497 biologically three independent experiments. (no. of GUVs = more than 30). **f.** Schematic
498 representation and XYZ Projection of the mycobacteria-mediated curvature change from e. **g.** Mean
499 fluorescence recovery curve after photobleaching experiments of direct contact of bacteria on the
500 membrane. Data points using mean values from three independent experiments. Scale bar, 5µm **h.**
501 Time-lapse confocal imaging of GUVs of phagosomal membrane composition labelled with 0.05%
502 Rh-PE (red) and 0.05% Top Fluor cholesterol (green) and immobilized using 0.03% PEG-Biotin
503 encapsulated with live M. Smegmatis (green). Scale bar, 10µm. Images are the representation from
504 three independent experiments. (no. of GUVs = more than 30). Zoomed image of confocal images
505 of region near to direct contact of bacteria at **i.** 0 mins, **j.** 60 mins (Scale bar: 5µm.). White box in i
506 indicates the region for line intensity profile at respective time points. Fluorescence intensity profile
507 of **k.** green channel and **l.** red channel at two different time intervals.
508
509
510
511
512
513
514
515
516
517
518
519
520
521
522
523
524

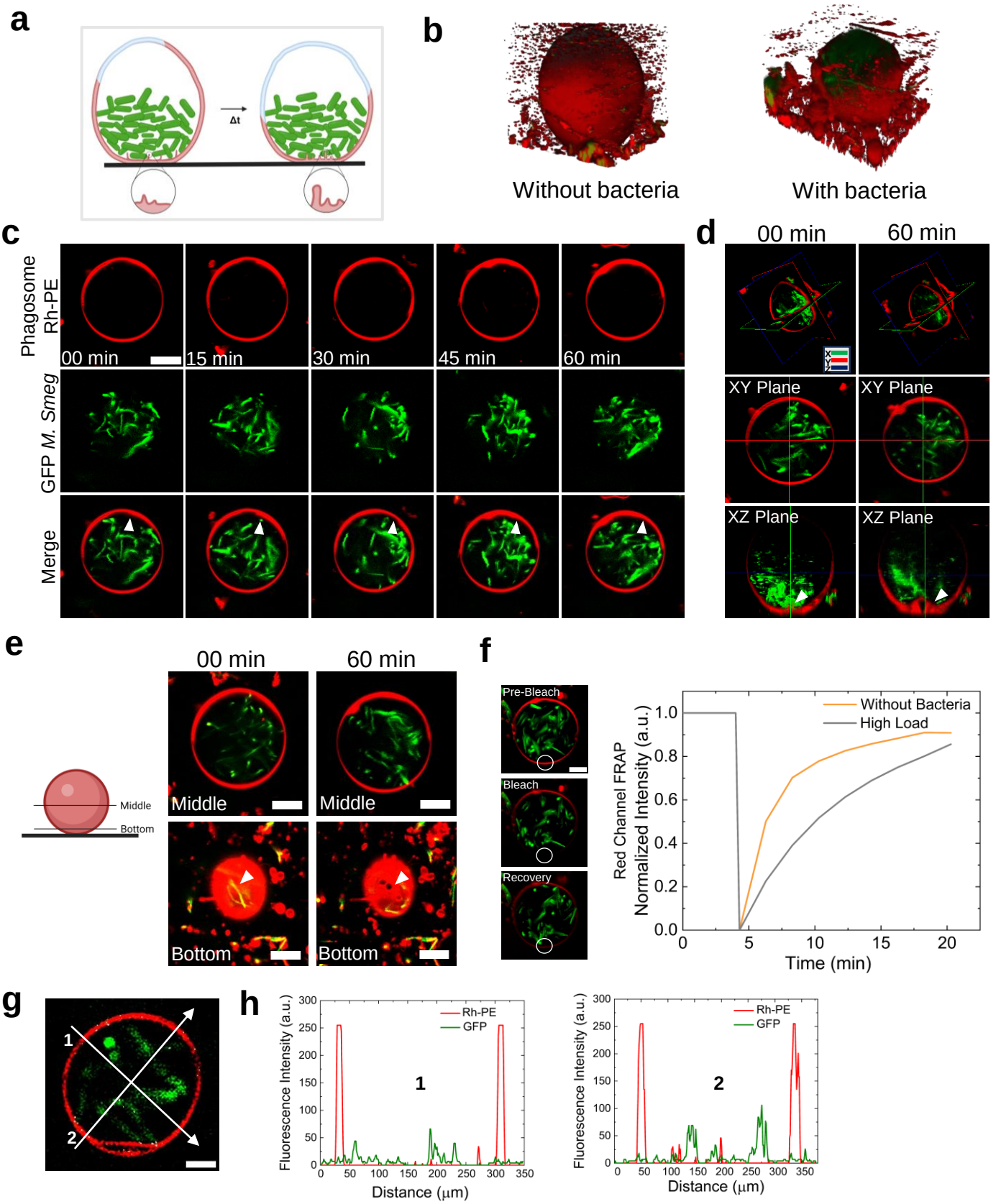
a
Δt
b
Without bacteria
With bacteria
c
Phagosome Rh-PE
GFP M. Smeg
Merge
00 min
15 min
30 min
45 min
60 min
d
00 min
60 min
XY Plane
XY Plane
XZ Plane
XZ Plane
e
00 min
60 min
Middle
Bottom
Middle
Middle
Bottom
Bottom
f
Pre-Bleach
Bleach
Recovery
Without Bacteria
High Load
Red Channel FRAP Normalized Intensity (a.u.)
Time (min)
g
1
2
h
Rh-PE
GFP
Fluorescence Intensity (a.u.)
Distance (μm)
1
2

Fig 2

Mycobacterial load induces phase separation in the phagosome membrane

a. Schematic representation for the experimental design depicting the impact of a moderate load of bacteria on immobilized GUV mimicking host phagosomal membrane. **b.** 3D projection of vesicle without and with bacteria exhibiting the bacteria-induced phase separation (no. of GUVs = more than 30). **c.** Time- lapse confocal imaging of GUVs labelled with 0.1% Rh-PE (red) and immobilized using 0.03% PEG-Biotin encapsulated with moderate load live *M. smegmatis* (green). Scale bar, 10µm. Representative images from biologically three independent experiments. (no. of GUVs = more than 30). **d.** XYZ Projection of the mycobacteria load mediated changes from c representing the budding event over time. **e.** Schematic representation and XY plane of the same GUV from c, representing different planes. **f.** Mean fluorescence recovery curve after photobleaching experiments of moderate loaded GUVs on the membrane. Data points using mean values from three independent experiments. Scale bar, 5µm **g.** Structured illumination microscopy (SIM) images of GUVs labelled with 0.1% Rh-PE (red) and immobilized using 0.03% PEG-Biotin encapsulated with moderate load of live *M. smegmatis* (green), 5µm. (no. of GUVs = more than 20). Line intensity plots in **h**. of line 1 and 2 respectively.

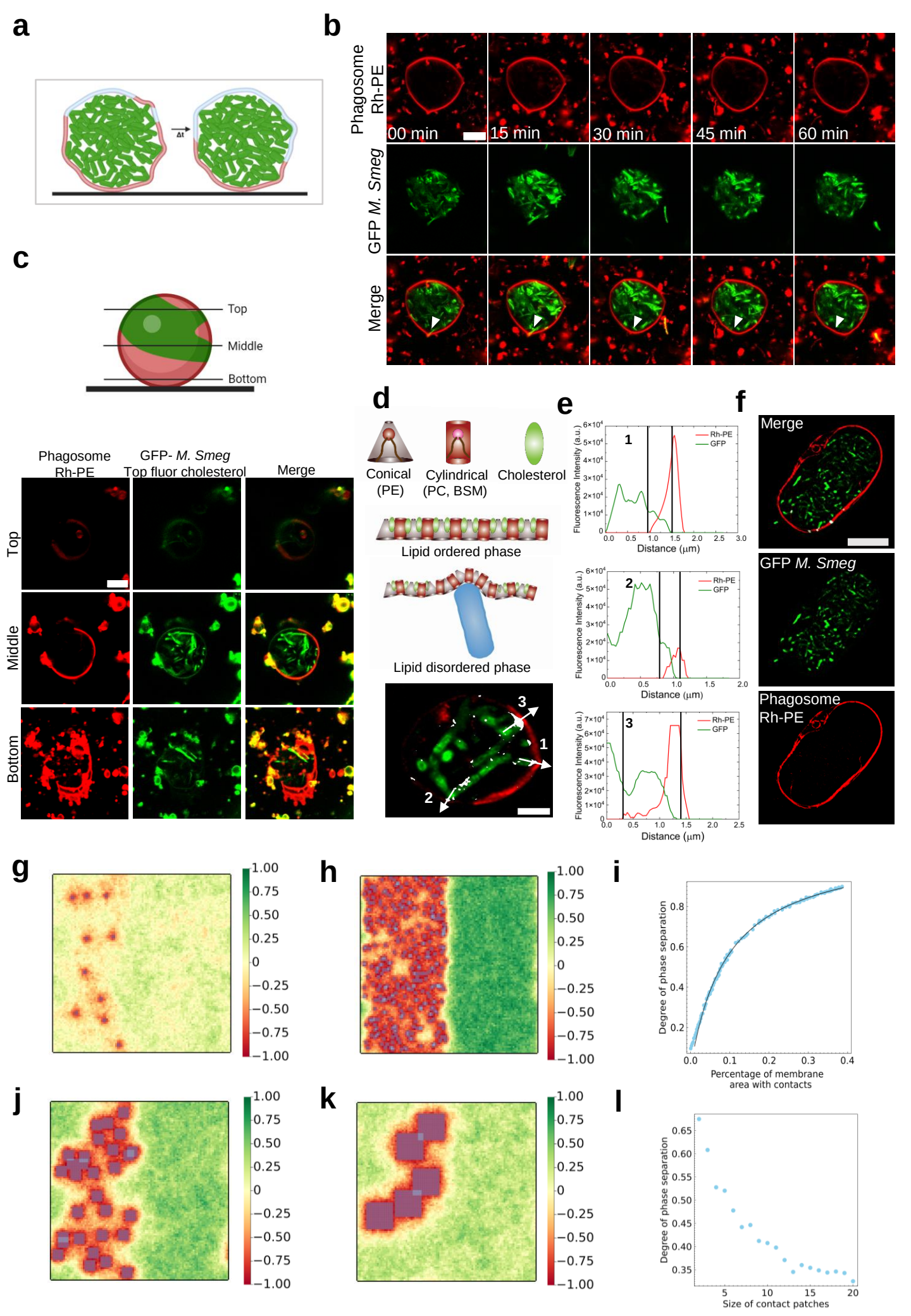
a
Δt
b
Phagosome Rh-PE
GFP M. Smeg
Merge
00 min
15 min
30 min
45 min
60 min
c
Top
Middle
Bottom
Phagosome Rh-PE
GFP- M. Smeg Top fluor cholesterol
Merge
Top
Middle
Bottom
d
Conical (PE)
Cylindrical (PC, BSM)
Cholesterol
Lipid ordered phase
Lipid disordered phase
1
2
3
e
Fluorescence Intensity (a.u.)
Distance (μm)
Rh-PE
GFP
f
Merge
GFP M. Smeg
Phagosome Rh-PE
g
h
i
Degree of phase separation
Percentage of membrane area with contacts
j
k
l
Size of contact patches

Fig 3

High mycobacterial load induces host membrane remodeling through condensation driven by bacterial surface interactions

a. Schematic representation for the experimental design depicting the impact of a high load of bacteria on immobilized GUV mimicking phagosomal membrane. **b.** Time-lapse confocal imaging of GUVs labelled with 0.1% Rh-PE (red) and immobilized using 0.03% PEG-Biotin encapsulated with high load of live *M. smegmatis* (green). Scale bar, 10µm. Representative images from biologically three independent experiments (no. of GUVs = more than 20). **c.** Schematic representation and XY plane of the GUV of phagosomal membrane composition labelled with 0.05% Rh-PE (red) and 0.05% Top Flor cholesterol (green) and immobilized using 0.03% PEG-Biotin encapsulated with high load of live *M. Smegmatis* (green) representing different planes. Scale bar, 10µm. Images are the representative of three independent experiments. (no. of GUVs = more than 20). **d**. Structured illumination microscopy (SIM) images of GUV, white spot showing degree of colocalization. **e.** showing line intensity graph plot for Rh-PE (red channel) and GFP (green channel) and marked area with black line denote overlapping region of red and green channel. For the colocalization the points are mentioned in d. **f.** Structured illumination microscopy (SIM) images of high loaded GUVs GUV remodels the shape of GUV (no. of GUVs = more than 20). Time-averaged state of the membrane. **g.** With a low load, phase separation is observed only near the contacts. Degree of phase separation 0.137 (N_c = 10, p=2). **h.** With a high load, global phase separation is seen. Degree of phase separation 0.675 (N_c=300, p=2). **i.** Degree of phase separation in the membrane as a function of the percentage of membrane area in contact with the membrane. **j,k,l.** Varying the contact patch size, keeping the fraction of membrane area in contact fixed. j & k show representative time-averaged states for p=6 and p=15 respectively. (Parameters in all figures: N=100, φ=0.5, J/k_BT=0.4, h/k_BT=5.0)

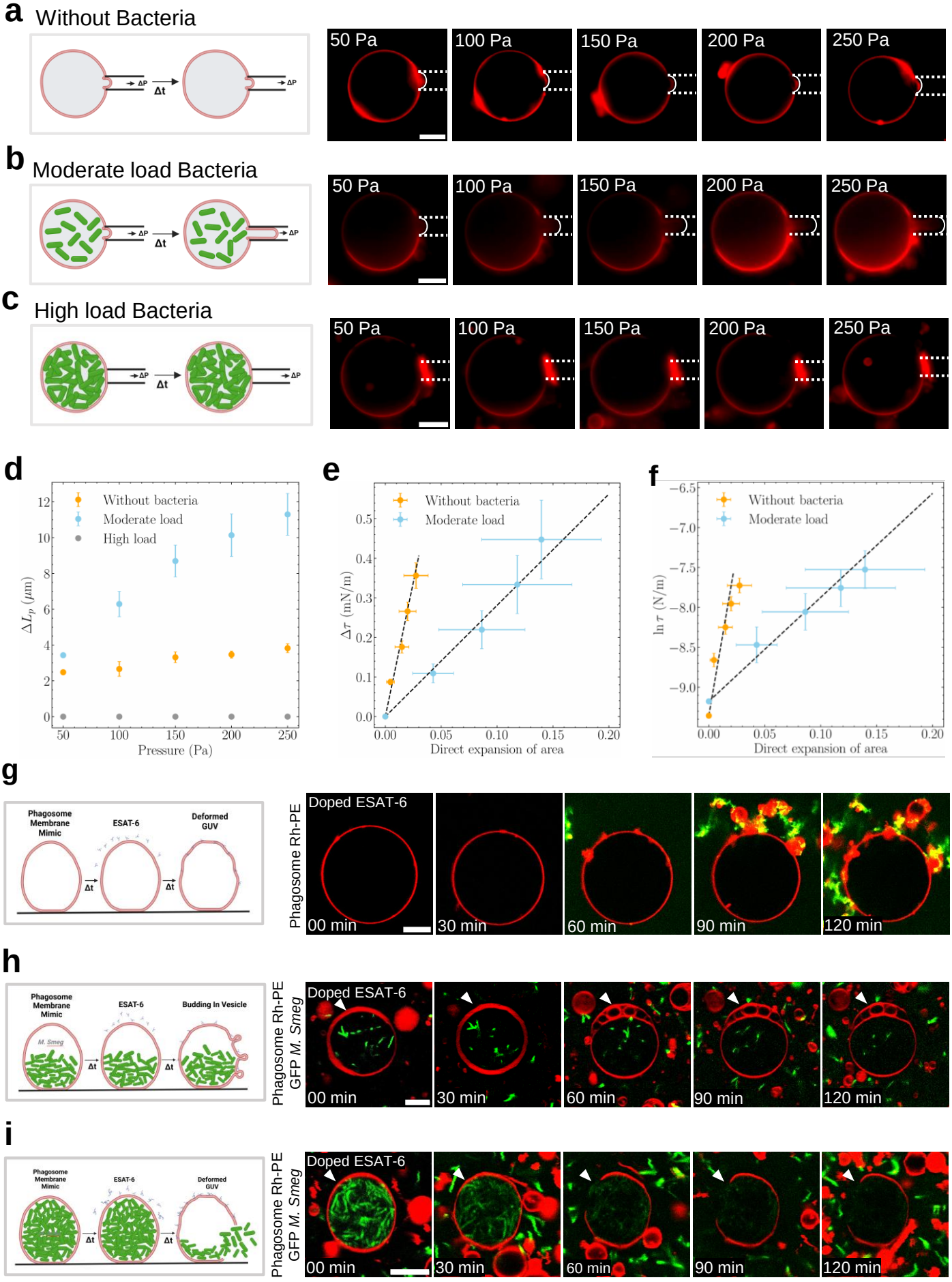
a
Without Bacteria
ΔP
Δt
ΔP
50 Pa
100 Pa
150 Pa
200 Pa
250 Pa
b
Moderate load Bacteria
ΔP
Δt
ΔP
50 Pa
100 Pa
150 Pa
200 Pa
250 Pa
c
High load Bacteria
ΔP
Δt
ΔP
50 Pa
100 Pa
150 Pa
200 Pa
250 Pa
d
Without bacteria
Moderate load
High load
ΔL_p (μm)
Pressure (Pa)
e
Without bacteria
Moderate load
$\Delta\tau$ (mN/m)
Direct expansion of area
f
Without bacteria
Moderate load
$\ln\tau$ (N/m)
Direct expansion of area
g
Phagosome Membrane Mimic
ESAT-6
Deformed GUV
Δt
Δt
Phagosome Rh-PE
Doped ESAT-6
00 min
30 min
60 min
90 min
120 min
h
Phagosome Membrane Mimic
ESAT-6
Budding In Vesicle
M. Smeg
Δt
Δt
Phagosome Rh-PE
GFP M. Smeg
Doped ESAT-6
00 min
30 min
60 min
90 min
120 min
i
Phagosome Membrane Mimic
ESAT-6
Deformed GUV
Δt
Δt
Phagosome Rh-PE
GFP M. Smeg
Doped ESAT-6
00 min
30 min
60 min
90 min
120 min

Fig 4

Direct contact with mycobacteria induces the virulence of ESAT-6.

a. Schematic representation and time-lapse Epi-fluorescence imaging of GUVs labelled with 0.1% Rh-PE (red). Scale bar, 10µm. Aspirated with Pressure (Δp=50Pa) and monitored over time. Representative images from biologically three independent experiments. **b.** Schematic representation and time-lapse Epi-fluorescence imaging of GUVs labelled with 0.1% Rh-PE (red) encapsulated with moderate load of live *M. smegmatis* (green). Scale bar, 10µm. Aspirated with Pressure (Δp=50Pa) and monitored over time. Representative images from biologically three independent experiments. **c.** Schematic representation and Time-lapse Epi-fluorescence imaging of GUVs labelled with 0.1% Rh-PE (red) encapsulated with high load live *M. smegmatis* (green). Scale bar, 10µm. Aspirated with Pressure (Δp=50Pa) and monitored over time. Representative images from biologically three independent experiments. **d.** Plot for the length of protrusion(ΔL_P) vs pressure (P) from a,b and c. Data points shown are the Means ± SD of three independent experiment. **e.** Quantifying the area stretch modulus(k_a) from the change in tension(Δτ) vs direct expansion of area plot from a, b and c. Orange and blue spots with bars: experimental points for without bacteria and moderate load, respectively, average ± SD. Dotted line: Linear fit, y= a*x+b, for without bacteria a = 13.5 ± 1.09, b = (-1.25 ± -0.49)*10^{-6} , R^2 = 0.125 and for moderate load a = 2.81 ± 0.10 b.(-1.81 ± 0.727)*10^{-7}, R^2 = 0.056455, $K_{a(\text{without load bacteria})}$ = 13.5 ± 1.09mN/m $K_{a(\text{Moderate load bacteria})}$ = 2.81 ± 0.10 mN/m **f.** Quantification of the bending modulus (k_b) from the semi-log plot of tension versus direct expansion of area from a, b, c. Orange and blue spots with bars: experimental points for without bacteria and moderate load, respectively, average ± SD. Dotted line: Linear fit y= a*x+b, for without bacteria a = 81.52 ± 1.489 , b = -2.45 ± (6.74*10^{-6}), R^2 = 0.605 and for moderate load a = 13.021 ± 0.9696, b = -2.27 ± (4.28*10^{-7}), R^2 =- 0.097, $K_{b(\text{without load bacteria})}$ =(1.33 ± 0.022)*10^{-20} J, $K_{b(\text{moderate load bacteria})}$ = (0.21±0.02)*10^{-20} J **g.** Time-lapse confocal imaging of GUVs labelled with 0.1% Rh-PE (red) and immobilized using 0.03% PEG-Biotin incubated with 2.5µM doped FITC-ESAT-6 (green). Scale bar, 10µm.Images are representative of 3 independent experiments (no. of GUVs = more than 30). **h.** Time-lapse confocal imaging of GUVs labelled with 0.1% Rh-PE (red) and immobilized using 0.03% PEG-Biotin encapsulated with moderate load of live *M. smegmatis* (green) and incubated with 2.5µM doped FITC-ESAT-6 (green). Scale bar, 10µm.Images are representative of 3 independent experiments (no. of GUVs = more than 30). **i.** Time-lapse confocal imaging of GUVs labelled with 0.1% Rh-PE (red) and immobilized using 0.03% PEG-Biotin encapsulated with high load of live *M. smegmatis* (green) and incubated with 2.5µM doped FITC-ESAT-6 (green). Scale bar, 10µm (no. of GUVs = more than 10).

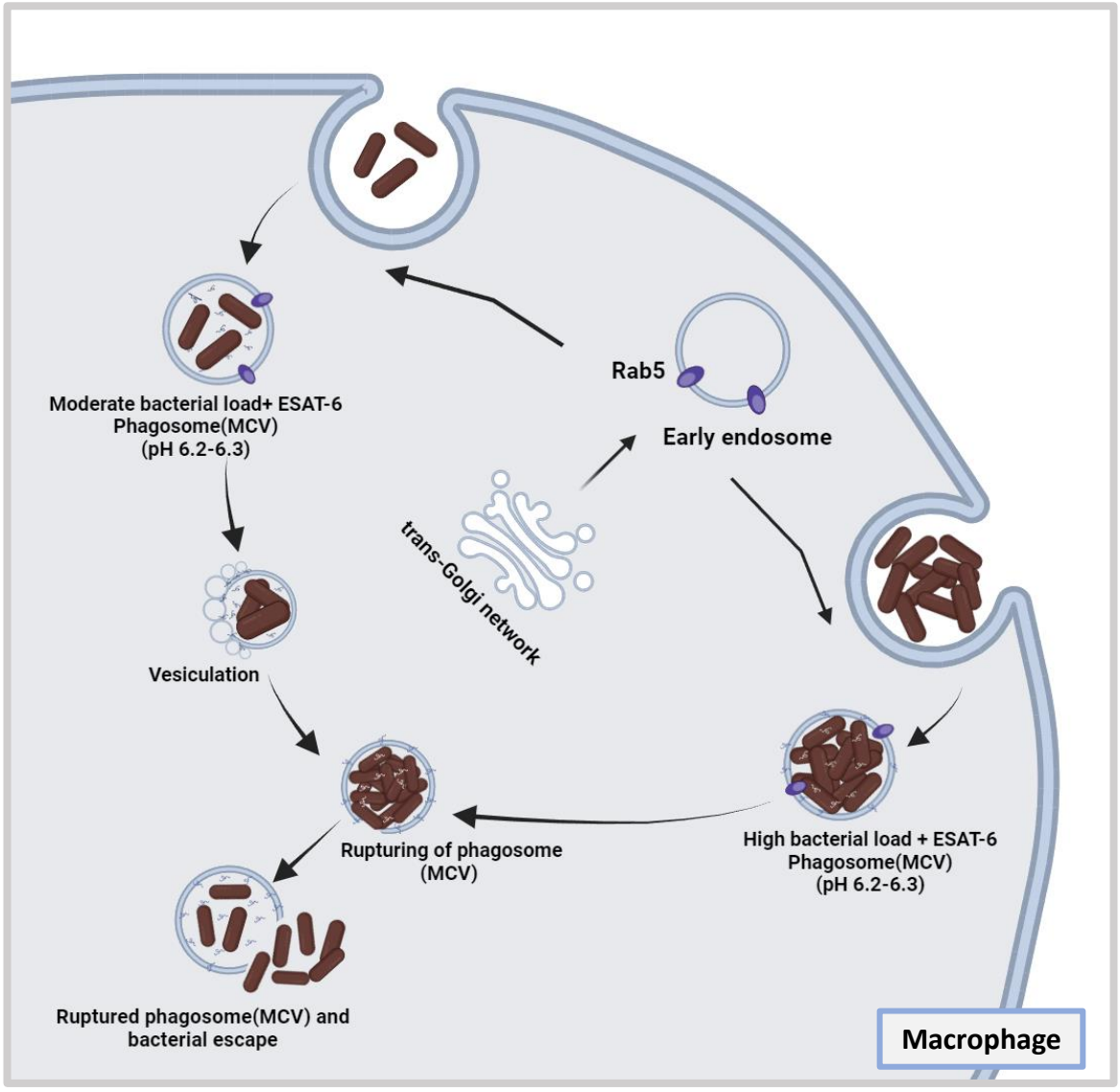
Moderate bacterial load+ ESAT-6
Phagosome(MCV)
(pH 6.2-6.3)
Rab5
Early endosome
trans-Golgi network
Vesiculation
Rupturing of phagosome
(MCV)
High bacterial load + ESAT-6
Phagosome(MCV)
(pH 6.2-6.3)
Ruptured phagosome(MCV) and
bacterial escape
Macrophage

Fig 5

Schematic representation of the proposed mechanism of direct contact of mycobacteria enhances the virulence of ESAT-6

695 **References**

696 1. Cossart, P. & Sansonetti, P.J. Bacterial invasion: the paradigms of enteroinvasive pathogens.
697 *Science (New York, N.Y.)* **304**, 242-248 (2004).
698 2. Galán, J.E. & Collmer, A. Type III secretion machines: bacterial devices for protein delivery
699 into host cells. *Science (New York, N.Y.)* **284**, 1322-1328 (1999).
700 3. Pizarro-Cerdá, J. & Cossart, P. Bacterial adhesion and entry into host cells. *Cell* **124**, 715-727
701 (2006).
702 4. Riethmüller, J., Riehle, A., Grassmé, H. & Gulbins, E. Membrane rafts in host-pathogen
703 interactions. *Biochimica et biophysica acta* **1758**, 2139-2147 (2006).
704 5. Eierhoff, T. *et al.* A lipid zipper triggers bacterial invasion. **111**, 12895-12900 (2014).
705 6. Veiga, E. *et al.* Invasive and adherent bacterial pathogens co-Opt host clathrin for infection.
706 *Cell host & microbe* **2**, 340-351 (2007).
707 7. Kühbacher, A. *et al.* Genome-Wide siRNA Screen Identifies Complementary Signaling
708 Pathways Involved in Listeria Infection and Reveals Different Actin Nucleation Mechanisms
709 during Listeria Cell Invasion and Actin Comet Tail Formation. *mBio* **6**, e00598-00515 (2015).
710 8. Pieters, J. Mycobacterium tuberculosis and the macrophage: maintaining a balance. *Cell host*
711 *& microbe* **3**, 399-407 (2008).
712 9. Augenstreich, J. *et al.* The conical shape of DIM lipids promotes Mycobacterium tuberculosis
713 infection of macrophages. *Proceedings of the National Academy of Sciences of the United*
714 *States of America* **116**, 25649-25658 (2019).
715 10. Hagedorn, M., Rohde, K.H., Russell, D.G. & Soldati, T. Infection by tubercular mycobacteria
716 is spread by nonlytic ejection from their amoeba hosts. *Science (New York, N.Y.)* **323**, 1729-
717 1733 (2009).
718 11. Gerstenmaier, L. *et al.* The autophagic machinery ensures nonlytic transmission of
719 mycobacteria. *Proceedings of the National Academy of Sciences of the United States of*
720 *America* **112**, E687-692 (2015).
721 12. Simeone, R., Sayes, F., Lawarée, E. & Brosch, R. Breaching the phagosome, the case of the
722 tuberculosis agent. *Cellular microbiology* **23**, e13344 (2021).
723 13. Russell, D.G. Who puts the tubercle in tuberculosis? *Nature reviews. Microbiology* **5**, 39-47
724 (2007).
725 14. Russell, D.G. Mycobacterium tuberculosis: here today, and here tomorrow. *Nature reviews.*
726 *Molecular cell biology* **2**, 569-577 (2001).
727 15. Bussi, C. & Gutierrez, M.G. Mycobacterium tuberculosis infection of host cells in space and
728 time. *FEMS microbiology reviews* **43**, 341-361 (2019).
729 16. Gröschel, M.I., Sayes, F., Simeone, R., Majlessi, L. & Brosch, R. ESX secretion systems:
730 mycobacterial evolution to counter host immunity. *Nature reviews. Microbiology* **14**, 677-
731 691 (2016).
732 17. van der Wel, N. *et al.* M. tuberculosis and M. leprae translocate from the phagolysosome to
733 the cytosol in myeloid cells. *Cell* **129**, 1287-1298 (2007).
734 18. Houben, D. *et al.* ESX-1-mediated translocation to the cytosol controls virulence of
735 mycobacteria. *Cellular microbiology* **14**, 1287-1298 (2012).
736 19. Simeone, R. *et al.* Phagosomal rupture by Mycobacterium tuberculosis results in toxicity and
737 host cell death. *PLoS pathogens* **8**, e1002507 (2012).
738 20. De Leon, J. *et al.* Mycobacterium tuberculosis ESAT-6 exhibits a unique membrane-
739 interacting activity that is not found in its ortholog from non-pathogenic Mycobacterium
740 smegmatis. *The Journal of biological chemistry* **287**, 44184-44191 (2012).

741 21. Kennedy, G.M., Hooley, G.C., Champion, M.M., Mba Medie, F. & Champion, P.A. A novel ESX-
742 1 locus reveals that surface-associated ESX-1 substrates mediate virulence in
743 Mycobacterium marinum. *Journal of bacteriology* **196**, 1877-1888 (2014).
744 22. Raffetseder, J., Iakobachvili, N., Loitto, V., Peters, P.J. & Lerm, M. Retention of EsxA in the
745 Capsule-Like Layer of Mycobacterium tuberculosis Is Associated with Cytotoxicity and Is
746 Counteracted by Lung Surfactant. *Infection and immunity* **87** (2019).
747 23. Conrad, W.H. *et al.* Mycobacterial ESX-1 secretion system mediates host cell lysis through
748 bacterium contact-dependent gross membrane disruptions. *Proceedings of the National*
749 *Academy of Sciences of the United States of America* **114**, 1371-1376 (2017).
750 24. Lerner, T.R. *et al.* Phthiocerol dimycocerosates promote access to the cytosol and
751 intracellular burden of Mycobacterium tuberculosis in lymphatic endothelial cells. *BMC*
752 *biology* **16**, 1 (2018).
753 25. Cambier, C.J., Banik, S.M., Buonomo, J.A. & Bertozzi, C.R. Spreading of a mycobacterial cell-
754 surface lipid into host epithelial membranes promotes infectivity. *eLife* **9** (2020).
755 26. Augenstreich, J. *et al.* ESX-1 and phthiocerol dimycocerosates of Mycobacterium
756 tuberculosis act in concert to cause phagosomal rupture and host cell apoptosis. *Cellular*
757 *microbiology* **19** (2017).
758 27. Barczak, A.K. *et al.* Systematic, multiparametric analysis of Mycobacterium tuberculosis
759 intracellular infection offers insight into coordinated virulence. *PLoS pathogens* **13**,
760 e1006363 (2017).
761 28. Astarie-Dequeker, C. *et al.* Phthiocerol dimycocerosates of M. tuberculosis participate in
762 macrophage invasion by inducing changes in the organization of plasma membrane lipids.
763 *PLoS pathogens* **5**, e1000289 (2009).
764 29. Lienard, J. *et al.* The Mycobacterium marinum ESX-1 system mediates phagosomal
765 permeabilization and type I interferon production via separable mechanisms. *Proceedings of*
766 *the National Academy of Sciences of the United States of America* **117**, 1160-1166 (2020).
767 30. Takatori, S.C. & Sahu, A. Active Contact Forces Drive Nonequilibrium Fluctuations in
768 Membrane Vesicles. *Physical review letters* **124**, 158102 (2020).
769 31. Dai, S. *et al.* Lipid Giant Vesicles Engulf Living Bacteria Triggered by Minor Enhancement in
770 Membrane Fluidity. *Nano letters* **23**, 371-379 (2023).
771 32. Le Nagard, L. *et al.* Encapsulated bacteria deform lipid vesicles into flagellated swimmers.
772 *Proceedings of the National Academy of Sciences of the United States of America* **119**,
773 e2206096119 (2022).
774 33. Sparks, I.L., Derbyshire, K.M., Jacobs, W.R., Jr. & Morita, Y.S. Mycobacterium smegmatis: The
775 Vanguard of Mycobacterial Research. *Journal of bacteriology* **205**, e0033722 (2023).
776 34. Baumgart, T., Hunt, G., Farkas, E.R., Webb, W.W. & Feigenson, G.W. Fluorescence probe
777 partitioning between Lo/Ld phases in lipid membranes. *Biochimica et biophysica acta* **1768**,
778 2182-2194 (2007).
779 35. Chakraborty, P., Bajeli, S., Kaushal, D., Radotra, B.D. & Kumar, A. Biofilm formation in the
780 lung contributes to virulence and drug tolerance of Mycobacterium tuberculosis. *Nature*
781 *communications* **12**, 1606 (2021).
782 36. Gohrbandt, M. *et al.* Low membrane fluidity triggers lipid phase separation and protein
783 segregation in living bacteria. *The EMBO journal* **41**, e109800 (2022).
784 37. Pandey, A.K. & Sassetti, C.M. Mycobacterial persistence requires the utilization of host
785 cholesterol. *Proceedings of the National Academy of Sciences of the United States of America*
786 **105**, 4376-4380 (2008).

38. Vutukuri, H.R. *et al.* Active particles induce large shape deformations in giant lipid vesicles. *Nature* **586**, 52-56 (2020).
39. Veatch, S.L. *et al.* Critical fluctuations in plasma membrane vesicles. *ACS chemical biology* **3**, 287-293 (2008).
40. Burns, M., Wisser, K., Wu, J., Levental, I. & Veatch, S.L. Miscibility Transition Temperature Scales with Growth Temperature in a Zebrafish Cell Line. *Biophysical journal* **113**, 1212-1222 (2017).
41. Gray, E., Karslake, J., Machta, B.B. & Veatch, S.L. Liquid general anesthetics lower critical temperatures in plasma membrane vesicles. *Biophysical journal* **105**, 2751-2759 (2013).
42. Gray, E.M., Díaz-Vázquez, G. & Veatch, S.L. Growth Conditions and Cell Cycle Phase Modulate Phase Transition Temperatures in RBL-2H3 Derived Plasma Membrane Vesicles. *PloS one* **10**, e0137741 (2015).
43. Rouches, M., Veatch, S.L. & Machta, B.B. Surface densities prewet a near-critical membrane. *Proceedings of the National Academy of Sciences of the United States of America* **118** (2021).
44. Sorre, B. *et al.* Curvature-driven lipid sorting needs proximity to a demixing point and is aided by proteins. **106**, 5622-5626 (2009).
45. Bosmani, C. *et al.* Membrane microdomains are crucial for Mycobacterium marinum EsxA-dependent membrane damage, escape to the cytosol and infection. 2024.2008. 2019.608731 (2024).
46. Levental, I. & Lyman, E. Regulation of membrane protein structure and function by their lipid nano-environment. *Nature reviews. Molecular cell biology* **24**, 107-122 (2023).
47. Kulakowski, G. *et al.* Lipid packing defects and membrane charge control RAB GTPase recruitment. *Traffic (Copenhagen, Denmark)* **19**, 536-545 (2018).
48. Saleem, M. *et al.* A balance between membrane elasticity and polymerization energy sets the shape of spherical clathrin coats. *Nature communications* **6**, 6249 (2015).
49. Kaksonen, M. & Roux, A. Mechanisms of clathrin-mediated endocytosis. *Nature reviews. Molecular cell biology* **19**, 313-326 (2018).
50. Larsen, J.B. *et al.* Membrane curvature enables N-Ras lipid anchor sorting to liquid-ordered membrane phases. *Nature chemical biology* **11**, 192-194 (2015).
51. Prince, A. *et al.* Lipid Specificity of the Fusion of Bacterial Extracellular Vesicles with the Host Membrane. *The journal of physical chemistry. B* **128**, 8116-8130 (2024).
52. Morlot, S. *et al.* Membrane shape at the edge of the dynamin helix sets location and duration of the fission reaction. *Cell* **151**, 619-629 (2012).
53. Evans, E. & Rawicz, W. Entropy-driven tension and bending elasticity in condensed-fluid membranes. *Physical review letters* **64**, 2094-2097 (1990).
54. Kwok, R. & Evans, E. Thermoelasticity of large lecithin bilayer vesicles. *Biophysical journal* **35**, 637-652 (1981).
55. Rawicz, W., Olbrich, K.C., McIntosh, T., Needham, D. & Evans, E. Effect of chain length and unsaturation on elasticity of lipid bilayers. *Biophysical journal* **79**, 328-339 (2000).

Acknowledgements

We thank Rohan Dhiman for the kind gift of the ESAT-6 plasmid and GFP-*M. smegmatis* strain. We thank Shubhay Arvind Dikkar and Sajag Kumar for their inputs during technical discussion. We acknowledge all the members of the M.S. lab for critical reading of the manuscript. SC is supported by the Ramalingaswami Re-entry Fellowship (BT/HRD/35/02/2006), Ministry of Science and technology, Government of India. MS gratefully acknowledges the DBT-Wellcome Trust India Alliance (Grant- IA/I/20/2/505212) and Department of Atomic Energy for financial support.